Si substituted hydroxyapatite nanorods on Ti for percutaneous implants

Kai Li, Yang Xue, Ting Yan, Lan Zhang**, Yong Han*

State-key Laboratory for Mechanical Behavior of Materials, Xi'an Jiaotong University, Xi'an, 710049, China

ARTICLE INFO

ABSTRACT

An ideal intraosseous transcutaneous implant should form a tight seal with soft tissue, besides a requirement of osseointegration at the bone-fixed position. Si substituted hydroxyapatite (Si-HA) nanorods releasing Si ion and simulating nanotopography of natural tissue were designed on Ti to enhance fibroblast response *in vitro* and biosealing with soft tissue *in vivo*. Si-HA nanorods were fabricated by alkali-heat treatment followed with hydrothermal treatment. The hydrothermal formation mechanism of Si-HA nanorods was explored. The surface characteristic of Si-HA nanorods was compared with pure HA nanorods. Fibroblast behaviors *in vitro* and skin response *in vivo* on different surfaces were also evaluated. The obtained results show that the substitution of Si did not significantly alter the phase component, morphology, roughness and wettability of HA, but additional Si and more Ca were released from Si-HA into medium. Comparing to pure HA nanorods and Ti substrate, Si-HA nanorods enhanced cell behaviors including proliferation, fibrotic phenotype and collagen secretion *in vitro*, and reduced epithelial down growth *in vivo*. The enhanced cell response and biosealing should be due to the releasing of Ca, Si and nanotopography of Si-HA nanorods. Si-HA nanorods can be a potential coating to accelerate skin integration for percutaneous implants in clinic.

1. Introduction

Titanium and its alloys have been widely used as intraosseous transcutaneous implants due to their excellent mechanical strength, corrosion resistance, chemical stability and biocompatibility [1–5]. However, Ti is bio-inert, and can't form biointegration with soft tissue. Marsupialization (epithelial downgrowth and pocket formation), avulsion (mechanically induced failure) and infection during the earlier phase of implantation always induce implant failure [2,6]. For an intraosseous transcutaneous Ti-based implant to be successful, it is critical to prevent epithelium recession and improve skin integration, besides osseointegration requirement at the bone-fixed position [4,7]. During skin-implant integration, fibroblasts play an important role as follows [8–12]. Once a wound is formed, fibroblasts adjacent to wound site are recruited and activated. They migrate, proliferate and secrete various growth factors including vascular endothelial growth factor (VEGF), basic fibroblast growth factor (b-FGF) and transforming growth factor (TGF)-β1 [11–13]. Simultaneously, they produce collagen I (Col-I)), synthesize collage matrix to form new connective tissue, and provide structural support for the wound [11,12]. In the remolding phase, they differentiate into a more contractile phenotype called myofibroblasts (characterized as alpha smooth muscle action (α-SMA)), which provide constant tension to contract the wound [12,14]. In order to enhance fibroblast response and the following skin integration of Ti implants, a number of coatings with different chemical compositions have been fabricated. Especially, hydroxyapatite not only improves osteoblast behavior and new bone formation [15,16], but also enhances fibroblast function and prevents skin recession [2,4]. It is known that natural skin tissue mainly consists of collagen fibrils and proteoglycan [10,12], and such a fibrous framework is an ideal extracellular matrix which can enhance cell response and remodel tissue dynamically [17,18]. In our previous work, HA nanorods simulating the nanotopography of natural tissue has been well explored to regulate osteoblast behavior and new bone formation on Ti implant [15,19,20], and they were also reported to enhance the fibroblast adhesion and proliferation when fabricated on zirconium [21]. It is known that Si plays a critical role in the attachment and differentiation of cells by activating focal adhesion kinase (FAK) [22,23], binds glycosaminoglycan forming cross-links between collagen and proteoglycan, and enhances osteoblast adhesion proliferation, differentiation and osseointegration [15,24–27]. Recently, extracellular supplement of Ca and Si ions has been reported to increase fibroblasts in collagen type I synthesis and collagen

---

* Corresponding author.
** Corresponding author.

E-mail addresses: lan.zhang@mail.xjtu.edu.cn (L. Zhang), Yonghan@mail.xjtu.edu.cn (Y. Han).

secretion *in vitro* [28,29], and skin wound healing *in vivo* [30,31]. We assumed that Si substituted HA nanorods with distorted lattice can accelerate Ca and Si releasing efficiently, and they can enhance fibroblast behavior and the followed biosealing with soft tissue, compared to pure HA. It is the fact that porous coatings are easily invaded by bacteria [32], inducing a high risk of infection compared to a smooth surface. So, in this paper, Si-HA nanorods was prepared on polished Ti by alkali-heat treatment (AHT) followed with hydrothermal treatment (HT), rather than the well reported hybrid process of micro arc oxidation and HT [15]. The microstructures and properties of HA nanorods substituted with Si were compared with pure HA, and the formation mechanism of Si-HA nanorods was explored. The fibroblast (L-929) response on different surfaces *in vitro* and biosealing *in vivo* were evaluated. It is demonstrated that Si-HA nanorods enhanced fibroblast response and biosealing due to the nanotopography and ion releasing. Si-HA nanorods should be a potential coating to accelerate skin integration for percutaneous implants.

2. Experimental methods

2.1. Preparation of HA and Si-HA nanorods

Commercially pure Ti disks (ϕ 15 × 2 mm) and Ti pillars (ϕ 2 × 15 mm) for were employed as substrates for *in vitro* and *in vivo* assays, respectively. They were ground successively with 100#, 400#, and 1500# abrasive papers, then ultrasonically washed in a series of ethanol and deionized water after acetone. Subsequently, they were immersed in a 5 mol l^{-1} sodium hydroxide solution at 60 °C for 2 h. After being washed in deionized water and air dried, the samples were immersed in aqueous solution containing 0.1 M Ca-EDTA, 0.1 M NaH_2PO_4 and 0.01 M NaOH for HT at 240 °C for 24 h. The obtained samples were named as HA. For preparing the Si substituted HA nanorods (Si-HA), 0.2 M Na_2SiO_3 was extra added into the above HT solution, keeping the same hydrothermal treatment condition. All hydrothermally treated samples were washed with distilled water and dried at room temperature.

2.2. Characterization of HA and Si-HA nanorods

The scanning electron microscope (SEM, SU6600, Hitachi, Japan) equipped with energy-dispersive X-ray spectrometer (EDX) was conducted to obtain the morphologies and compositions of the coatings. The X-ray diffraction (XRD) patterns were obtained on a Rigaku D/Max-2500VPC X-ray diffractometer with Ni-filtered Cu Ka radiation from 20° to 70° at a scanning rate of 0.02° s^{-1}. Transmission electron microscopy (TEM) analysis was conducted using a JEOL JEM-2100F electron microscope operating at 200 kV. The chemical species of HA and Si-HA coatings were examined with X-ray photoelectron spectroscope (XPS; Axis Ultra, U.K.). The obtained XPS spectra were corrected to the C 1s (hydrocarbon C/C, C/H) contribution at the binding energy of 284.6 eV.

HA and Si-HA were immersed in 10 mL 0.9 wt% NaCl aqueous solution at 37 °C for different days successively to obtain releasing kinetics of Ca and Si. At the pre-determined time points, the leaching liquid was collected and the concentrations of Ca and Si ions released were measured by inductively coupled plasma-mass spectrometry (ICP-MS; Nu Instruments, Wrexham, UK). Meanwhile, the Ca and Si ions concentrations in fresh NaCl aqueous solution were measured as the background. Three samples of each coating at each immersing time were measured to obtain an average value.

2.3. Protein adsorption assay

Total protein adsorption on different surfaces (Ti, HA, and Si-HA) was evaluated. Each sample was placed in a 24-well plate with 500 μL of α-MEM (Hyclone, USA) containing 10% fetal bovine serum (Genimi,

USA) and incubated at 37 °C for 4 and 24 h. Then, they were washed with phosphate buffer solution (PBS) three times and transferred to new wells. And then 500 μL of 1% sodium dodecyl sulfate (SDS) solution was added in each well, and the samples were shaken for 15 min. Finally, the concentrations of total protein were determined by a MicroBCA protein assay kit (Pierce, USA) according to the operation manual.

2.4. In vitro fibroblast response evaluation

A mouse fibroblast cell line (L-929), was purchased from the Institute of Biochemistry and Cell Biology of Chinese Academy of Sciences (Shanghai, China). The cells were inoculated into α-MEM (Hyclone, USA) containing 15 mM $NaHCO_3$, 10% fetal bovine serum (Genimi, USA), and, 1 mM sodium pyruvate (Sigma, USA), and incubated at 37 °C in an incubator with 5% CO_2 and 95% air. The complete medium was refreshed every two days.

2.4.1. Cell viability assay and morphology observation

Fibroblasts (2 × 10^4 cells per cm^2) were seeded on different surfaces and incubated for 1, 3, and 7 days, respectively. Viability and proliferation of fibroblasts were assessed by cell counting kit-8 (CCK-8) assay according to instruction.

Fluorescence staining of actin and cell nucleus was performed with a staining kit (Millipore, USA) as follows. After 24 h of culture, the cells seeded on different surface were fixed using 4% paraformaldehyde, and permeabilized using 0.1% Triton X-100 (Sigma, USA). Then 37.5 ng/mL tetramethyl rhodamine isothiocyanate conjugated phalloidin was added and cells were incubated at 37 °C for 60 min for staining of actin. For staining cell nucleus, 50 ng/mL 6-diamidino-2-phenylindole (DAPI) was subsequently added in each well and cells were incubated in at 37 °C for 5 min. Following each of the staining procedures, the samples were washed three times with 500 μL PBS buffer. The fluorescence-stained cells were observed by an epifluorescence (SMZ745T, Nikon, Japan).

2.4.2. Fibrogenic-related gene expressions by quantitative real-time PCR (qRT PCR) assay

After culturing fibroblasts for 3 and 7 days, the total RNA was isolated from the cells on each sample using the TRIzol reagent (Life Technologies, USA), and 1000 ng of RNA was reversed transcribed into complementary DNA using a Transcriptor First Strand cDNA Synthesis Kit (Roche, Switzerland). The expression of key fibrogenic differentiation markers (α-SMA, CTGF, TGF-β1, and Col-I) was quantified on a LightCycler 96 real-time PCR instrument (Roche, Switzerland) with SYBR FastStart Essential DNA Green Master Mix (Roche, Switzerland). All the qPCR reactions were normalized using the CT values corresponding to the housekeeping gene glyceraldehyde-3-phosphate dehydrogenase (GAPDH) through the $2^{-\Delta\Delta CT}$ method. No-template controls and melting curve analyses were included for each gene and PCR reaction. All analyses were repeated thrice using three replicates. The primers for the target genes and annealing temperatures were listed in Table 1.

2.4.3. Extracellular collagen secretion

After 3 and 7 days of culture, collagen secretion by fibroblasts on different samples was quantified by Sirius Red staining. Briefly, at each incubation time, the cell seeded samples were fixed in 4% paraformaldehyde, and stained in a saturated picric acid solution containing 0.1% Sirius Red (Sigma, USA) for 18 h. For quantitative analysis, the stain on the samples was eluted in 0.5 mL of destain solution (0.2 M NaOH/methanol 1:1), and then the optical density at 540 nm was measured using a spectrophotometer.

Table 1
Primers used for qRT-PCR, the corresponding annealing temperatures and product size.

Gene	Forward primer sequence (5′–3′)	Forward primer sequence (5′–3′)	Annealing temperature (°C)	Product size (bp)
α-SMA	CCTGAAGAGCATCCGACACT	AGAGTCCAGCACAATACCAGT	62	174
CTGF	CCTACCGCGTCCCGATCAT	GAGAGCGAGGAGCACCAAG	60	71
TGF-β1	AGGAGACGGAATACAGGGCT	TTTGGGGCTGATCCCGTTG	60	97
Col-I	ACGCCATCAAGGTCTACTGC	CGTACTCGAACGGGAATCCA	59	162
GAPDH	CCACCCTGTTGCTGTAGCC	CCCACTCCTCCACCTTTGA	60	105
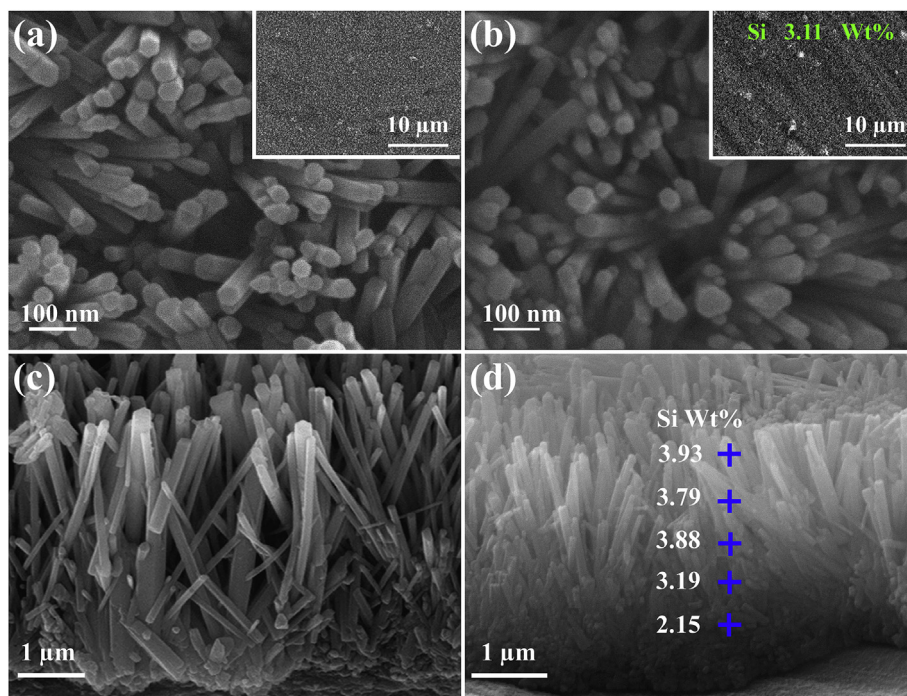
Fig. 1. Surface and cross-sectional SEM morphologies of the (a, c) HA, (b, d) Si-HA coatings.
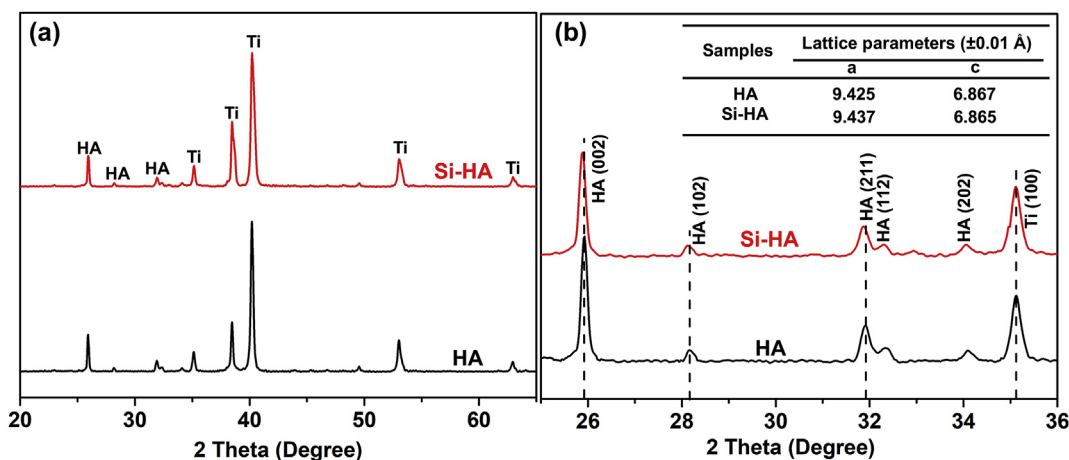
Fig. 2. (a) XRD patterns of HA and Si-HA, (b) an enlarged view of XRD pattern in the 25-36° of 2θ for HA and Si-HA. (Inset shows the lattice parameters (a and c) of hydroxyapatite for HA and Si-HA coatings.).

2.5. In vivo experiments

All the animal experiments were conducted according to the ISO 10993-2: 1992 animal welfare requirements, and all the experimental procedures were approved by the Institutional Animal Care and Use Committee of Xi'an Jiaotong University. Eight-week-old male C57BL/6 mice from the experimental animal center of the Fourth Military Medical University were used to evaluate the skin integration of the coated and pure Ti pillars. The mice were anesthetized by an intramuscular injection of 2.5 wt% pentobarbital sodium solution. For skin integration evaluation, each mouse was implanted with 3 pillars, as shown in Fig. S1 (a). The operation process and the entire region containing the implants was harvested for histological examination as detailed in previous work [7,33]. The areas of interest within the cutaneous part of the implant are schematically shown in Fig. S1(b). Digital microscopic images were captured on a microscopy (SMZ745T,
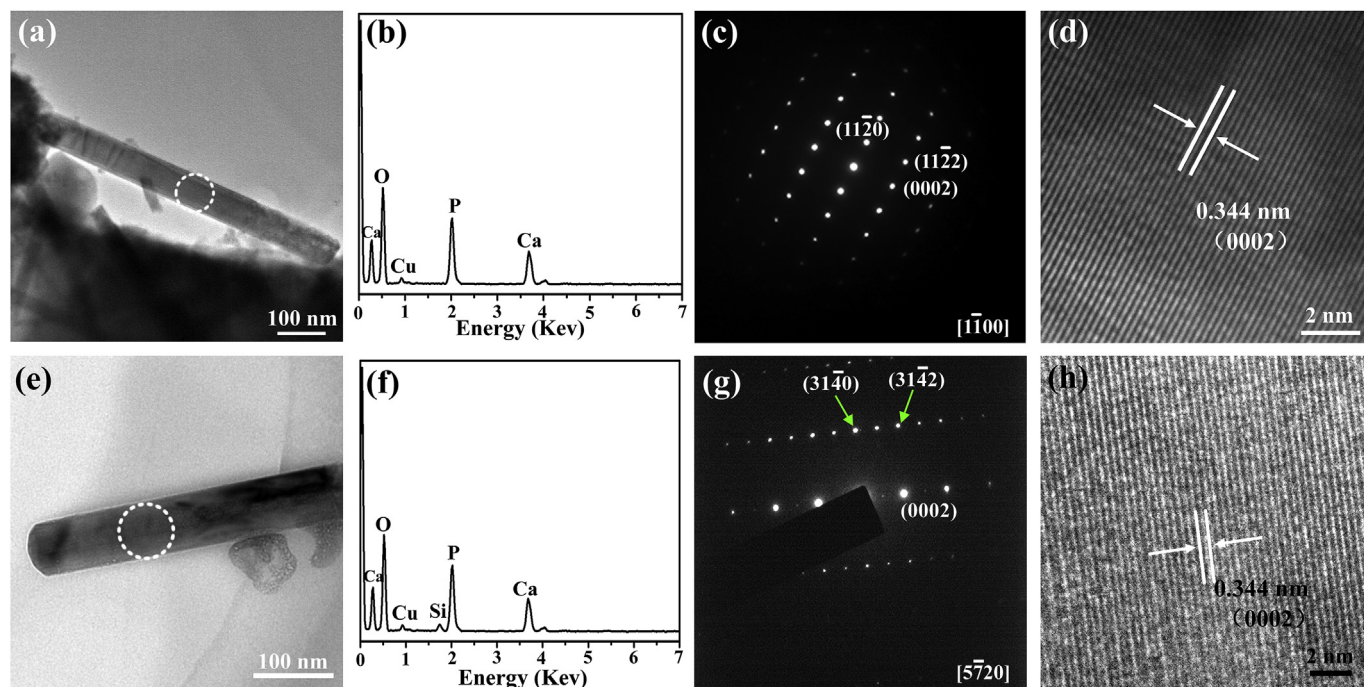
Fig. 3. TEM images of scratched nanorods from the surfaces of HA (a)–(d) and Si-HA (e)–(h): (a) and (e) bright-field images; (b) and (f) EDS patterns taken from the area marked with a ring in (a) and (e), respectively; (c) and (g) the corresponding SAED of (a) and (e), respectively; (d) and (h) HRTEM images of the nanorods marked with a ring in (a) and (e), respectively.
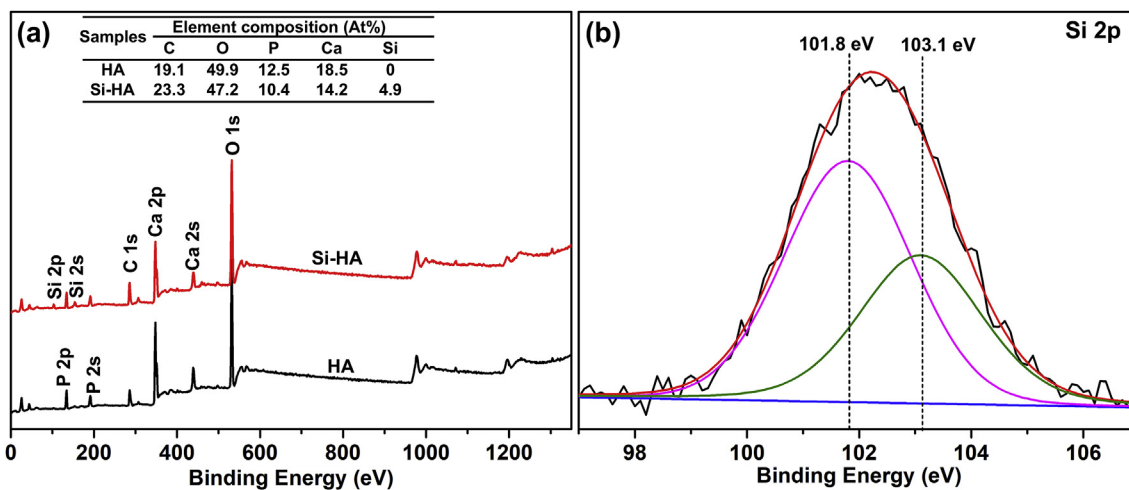
Fig. 4. XPS patterns of the different samples: (a) survey, (b) Si 2p.

Nikon, Japan).

2.6. Statistical analysis

The data were analyzed using SPSS 14.0 software (SPSS, USA). A one-way ANOVA followed by a Student–Newman–Keuls posthoc test was used to determine the level of significance. $P < 0.05$ was considered to be significant, and $p < 0.01$ was considered to be highly significant. All the data are presented as the mean $\pm$ standard deviation (SD).

3. Results

3.1. Structure of the hydrothermally treated coatings

Fig. 1 shows the surface and cross-sectional morphologies of HA and Si-HA coatings. Nanorods are hexagonal with an average diameter of 70 nm and an inter-rod spacing of 130 nm (Fig. 1(a) and (b)), and they vertically grow on Ti substrate. The lengths of HA and Si-HA nanorods are both about 3 μm (Fig. 1 (c) and (d)). Si element (3.11 wt%) were additionally detected on Si-HA (Fig. 1(b)) besides the other elements on HA. Its average content slightly decreases from nanorod tops to the bottoms (Fig. 1(d)). The XRD patterns show that the two coatings have the same peaks. The peaks at 25.88°, 28.97°, 31.77°, and 32.90° are corresponded to (002), (102), (211), and (300) crystal planes of hydroxyapatite (JCPDS No. 9-432), respectively (Fig. 2(a)). Compared with HA, some diffraction peaks (e.g. (002) and (211)) for Si-HA shift toward lower values and their full widths at half maximum slightly broaden (Fig. 2 (b)). The calculated *a*-axis of hydroxyapatite for Si-HA is slightly elongated compared to HA (Table inserted in Fig. 2(b)). Nanorods scratched from HA and Si-HA surfaces both show that they have average diameters of 70 nm (TEM images in Fig. 3(a) and (e)).
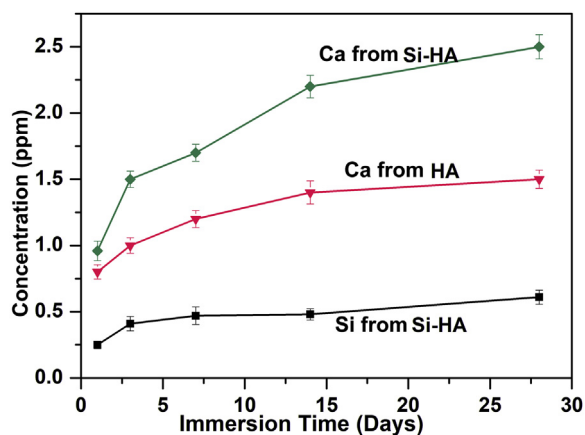
Fig. 5. Ca and Si release kinetics of HA and Si-HA after immersion for different days.

Besides Ca, P and O, Si was additionally detected in the nanorod from Si-HA (Fig. 3(b) and (f)). The nanorods are single-crystallized hydroxyapatite, as identified by the selected area electron diffraction (SAED) pattern (Fig. 3(c) and (g)) and their high-resolution TEM (HRTEM) images ((Fig. 3(d) and (h)).

In order to further explore the element composites and Si status in hydroxyapatite lattice, HA and Si-HA were detected by XPS, as shown in Fig. 4. HA consists of C, O, Ca and P, and Si-HA additionally contains Si beside the other elements on HA. It is further confirmed by the corresponding surface chemical compositions (Table inserted in Fig. 4(a)). The high-resolution spectrum of Si 2p peak on Si-HA is asymmetric and was deconvoluted into two components centered at 101.8 and 103.1 eV (Fig. 4(b)). 101.8 eV was assigned to the silicon atoms present in the orthosilicate anions SiO_4^{4-}, which occupied PO_4^{3-} anions in HA lattice, and 103.1 eV was assigned to three-dimensional silicates [15,19,34]. Based on the obtained results (Figs. 2–4), it is confirmed that substitution of Si does not change nanorod microstructure obviously, and Si replaces some P in hydroxyapatite lattice successfully, resulting in lattice distortion.

3.2. Ion release kinetics of HA and Si-HA

Ca and Si released from HA and Si-HA after immersion for 1–28 days were evaluated. For each coating, Ca revealed a fast-releasing stage within the initial 14 d followed by a slow release from 14 to 28 days (Fig. 5). At each immersion time, accumulated concentration of Ca released from Si-HA was higher than that from HA. Si gradually released from Si-HA, and after 28 days of immersion, the accumulated

concentration of Si is about 0.5 ppm.

3.3. Protein adsorption and in vitro fibroblast response evaluation

3.3.1. Protein adsorption assessment

The amounts of total protein adsorbed from culture medium on different surfaces after 4 and 24 h of incubation are shown in Fig. 6 (a). With the immersion time prolonged from 4 to 24 h, the protein amount adsorbed on each surface increased. At each immersion time, almost the same amounts of protein were adsorbed on HA and Si-HA surfaces, and they were much more than that on pure Ti.

3.3.2. Cell adhesion and proliferation assessment

After incubation for 1, 3 and 7 days, mitochondrial activity of L929 on different surfaces was evaluated and shown in Fig. 6 (b). After incubation for 1 day, the mitochondrial activity of cells followed the order: Si-HA > HA > Ti, indicating that the adhesion of cells on hydrothermally treated samples was higher than that on Ti. As the incubation was prolonged to 3 and 7 days, the mitochondrial activity on each surface significantly increased indicating the proliferation of cells. The proliferation of fibroblasts on Si-HA or Ti was significantly higher than that on HA.

To investigate the morphologies of cells seeded on the coatings, actin-nucleus staining fluorescence images after 1 and 3 days of culture were taken as shown in Fig. 7. After incubation for 1 day, most cells on Ti were spherically shaped. More cells adhered on hydrothermally treated surfaces, and they spread better, especially on Si-HA. It indicates that the nanorod topography and Si substitution in HA can enhance cell attachment. At 3 days of incubation, cells on all the surfaces showed typically spindle morphologies. They spread well and contacted with each other, indicating their good status, but less cells were observed on HA than on Si-HA and Ti, which was accordant to the mitochondrial activity result in Fig. 6(b).

3.3.3. Fibrogenic-related gene expression assessment and extracellular collagen secretion assessment

Expressions of fibrogenic-related genes including TGF-β1, CTGF, α-SMA and Col-I in the cells cultured on Ti, HA and Si-HA for 3 and 7 days were detected and shown in Fig. 8 (a)-(d). With the increased incubation time, gene expression on every surface increased, and at each incubation time, they followed the same order: Si-HA > HA > Ti. Collagen secretion of L929 on different coatings after 3 and 7 days of incubation was also evaluated. The quantified secretion of collagen at each incubation time was in the order: Si-HA > HA > Ti, and they tended to increase with the prolonged culture time from 3 to 7 days (Fig. 8(e)). It is further confirmed by the staining pictures of collagen secretion on different surfaces at 7 days of incubation (Fig. 8(f)).
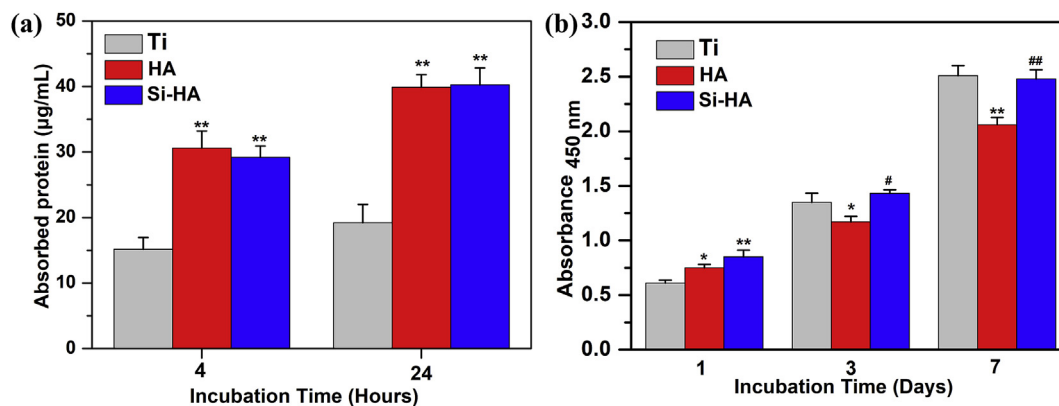
Fig. 6. (a) Total protein adsorbed onto different surfaces after 4 and 24 h of incubation in α-MEM containing 10% fetal bovine serum. (b) CKK8 assays of cell adhesion on different surfaces after 1 day, and proliferation after 3 and 7 days of incubation. Data are presented as the mean ± SD, n = 4, (*) p < 0.05 and (**) p < 0.01 compared with the Ti, (#) p < 0.05 and (##) p < 0.01 compared with HA.
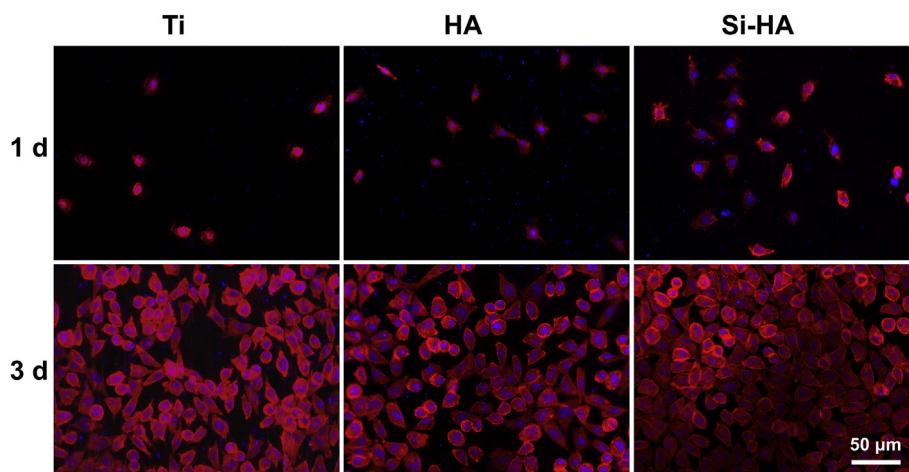
Fig. 7. Actin (red) and cell nucleus (blue) fluorescence images of fibroblasts after 1 and 3 days of culture on different surfaces.
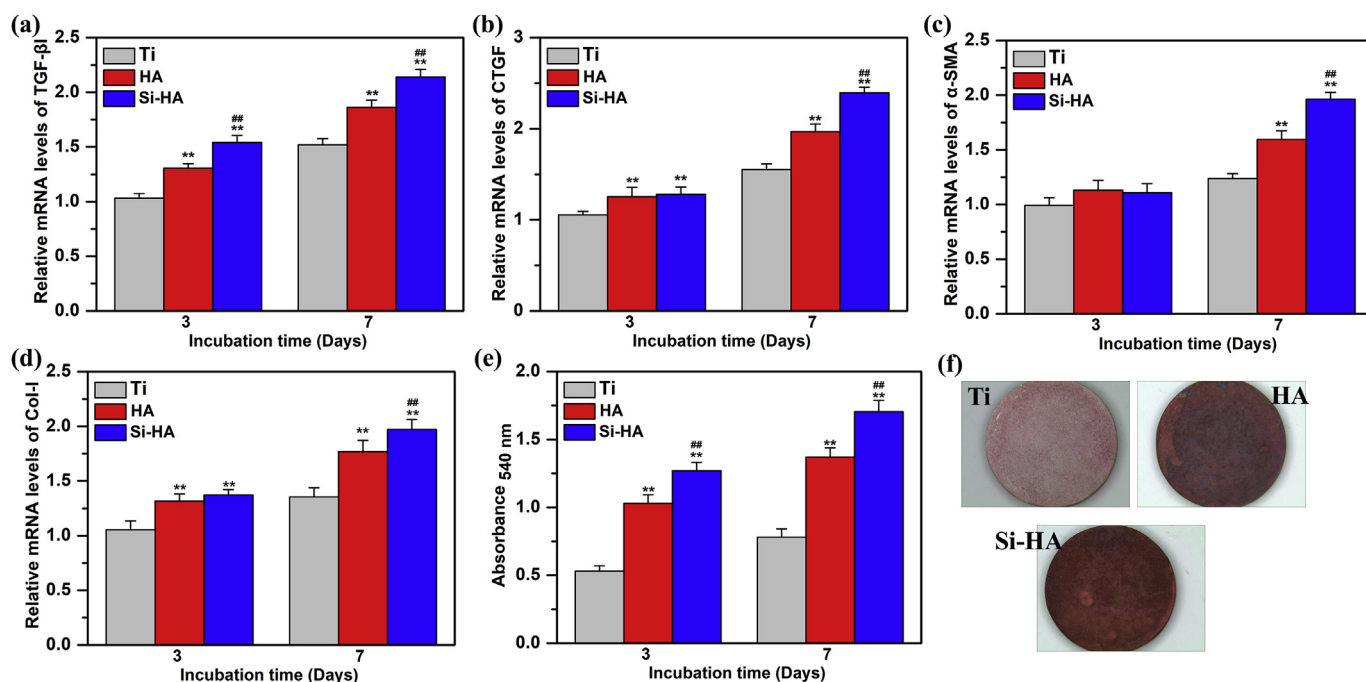
Fig. 8. Gene expressions of fibroblasts cultured on different surfaces after incubation for 3, and 7 days: (a) TGF-β1, (b) CTGF, (c) α-SMA, (d) Col-I; (e) collagen secretion of L929 determined with Sirius Red staining incubated on different coatings for 3 and 7 days; (f) staining pictures of collagen secretion at 7 days of incubation. Data are presented as the mean ± SD, n = 4, (**)p < 0.01 compared with the Ti, and (##)p < 0.01 compared with HA.

3.3.4. In vivo experiments

The integration of implant surfaces with skin *in vivo* for 4 weeks was evaluated, and Fig. 9 shows the histological strained images of different samples. For Ti, the skin migrated significantly along the implant surface (marked with the black squares in Fig. 9), leaving little skin adhered on the surface, and fibrous capsule (marked with the black line in Fig. 9) about 400 μm was formed around the implant. It indicates a weak integration between bare Ti and skin. For HA, although the skin down growth was obviously reduced as compared to Ti (marked with the red squares in Fig. 9), and the fibrous capsule was thinner (less than 100 μm, marked with the red line in Fig. 9), however, the epithelial down-growth was still serious. For Si-HA, skin migrated a little along the implant surface (marked with the blue squares in Fig. 9) and no fibrous capsule was formed around the implant, indicating a tighter seal between the underlying dermis and the implant surface.

4. Discussion

Hydroxyapatite nanorods cannot be formed on bare Ti just by HT treatment without pre-treatment in alkali solution (Fig. S2(a)). Porous nanonet can be formed after treatment in alkali solution (Fig. S2(b)), and they are sodium hydrogen titanate formed due to reaction of OH⁻ and Ti at outermost layer [35]. When sodium hydrogen titanate was hydrothermally treated in solution containing Ca^{2+}, OH^- and PO_4^{3-}, it could supply nucleation position for hydroxyapatite because of good lattice match [36]. Hydroxyapatite nuclei formed due to locally supersaturated concentrations of Ca^{2+}, OH^- and PO_4^{3-} and grew into nanorods according to the Ostwald ripening process with the prolonged HT process (Fig. S3) [37]. The formation mechanism of hydroxyapatite nanorods is shown in Fig. S4(a). When SiO_3^{2-} was extra added in HT solution, during the nanorod formation, SiO_3^{2-} took part in the nucleation and growth of hydroxyapatite, partially replacing PO_4^{3-} in hydroxyapatite lattice (Fig. S4(b)) and Si substituted hydroxyapatite
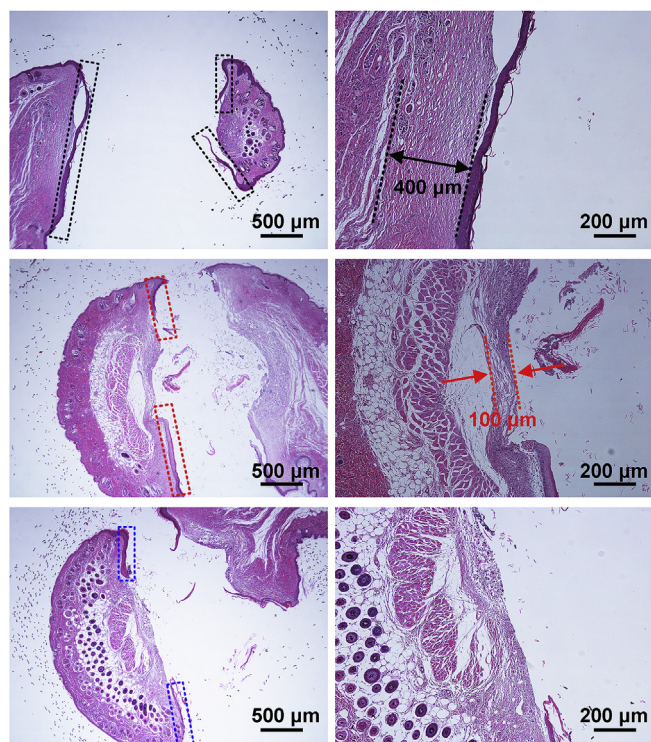
Fig. 9. Histological strained images of the pillar with different coatings, images in the right row showing the larger views of the area marked with rings in the left.

formed (Figs. 1–4). Due to substitution of Si, the crystal cell of hydroxyapatite had a small expansion in *a*-axis (Fig. 2), and lattice distortion accelerated Ca release during the immersion (Fig. 5).

When a percutaneous implant is penetrated the skin, proteins initially adsorb on its surface, followed by adhesion, proliferation, and differentiation of fibroblasts adjacent to wound site. The remodeling process of new skin around the implant is mainly decided by fibroblast response, which is related with surface properties. As is well known, surface properties include chemical composition, surface wettability, surface roughness and topography *etc.*. Nanorods and hydrophilic surfaces are reported to adsorb fibronectin (FN) and vitronectin (VN) from serum, efficiently [20,31]. FN and VN are the anchoring proteins required for integrin-receptor-based cell adhesion, and more hydrophilic surfaces lead the adsorbed FN and VN to be in a more bioactive conformation for cell adhesion [38,39]. So, cells adhered and spread better on hydrothermally treated surfaces than on pure Ti (Figs. 6 and 7). However, the proliferation of fibroblasts slightly decreased on HA compared with Ti, which may be due to the negative effect of inter-rod spacing (130 nm) on cell response. It is well explored that when the nanorod interspace is larger than 96 nm, cell proliferation is inhibited [15,20,40]. Si-HA has the similar phase composition, nanotopography, wettability and roughness (Figs. 1 and 2 and S5) with HA, but additional Si and more Ca can be released from Si-HA into medium (Fig. 5). So, the combined effect of ion and nanotopography should contribute to the improved behavior of L929 on Si-HA, including adhesion, proliferation and functional expression (Figs. 6–8). It is known that TGF-β1 induces collagen synthesis, enhances expression of α-SMA and CTGF and plays a key role in stimulating the differentiation of fibroblast into myofibroblast [11,41,42]. Nanorods released Si and/or Ca ions with enhanced mRNA levers of TGF-β1, CTGF, α-SMA and Col-I as well as collagen secretion, they reduced epithelial down growth, enhancing biosealing of implant with skin tissue (Fig. 9). The adhesion strengths of nanorods on HA and Si-HA are high enough for a coating on implant (Fig. S6) when serving *in vivo* [43]. It is demonstrated that

hydroxyapatite nanorods, especially the Si substituted, should be a potential coating to accelerate biosealing for percutaneous implants.

5. Conclusion

Si substituted hydroxyapatite nanorods were fabricated on Ti by a hybrid process of alkali-heat treatment and hydrothermal treatment. During the HT process, Ca^{2+} reacted with PO_4^{3-} and SiO_3^{2-} in HT solution, forming the HA nuclei on sodium hydrogen titanate, in which P was partially replaced by Si. The substitution of Si didn't alter phase component, morphology, roughness and wettability of nanorods obviously, but enhanced Ca and Si releasing. Hydroxyapatite nanorods especially the Si substituted improved functional expression of fibroblasts *in vitro* and reduced epithelial down growth *in vivo*. The combined effect of Ca and Si ions and nanotopography of hydroxyapatite nanorod contributed the enhanced cell response *in vitro* and biosealing *in vivo*.

CRediT authorship contribution statement

Kai Li: Software, Data curation, Validation, Writing - original draft, Methodology. **Yang Xue:** Validation, Software. **Ting Yan:** Visualization, Investigation, Methodology. **Lan Zhang:** Conceptualization, Writing - review & editing. **Yong Han:** Supervision.

Declaration of competing interest

The authors declare that they have no known competing financial interests or personal relationships that could have appeared to influence the work reported in this paper.

Acknowledgements

Appendix A. Supplementary data

Supplementary data to this article can be found online at https://doi.org/10.1016/j.bioactmat.2020.01.001.

References

[1] M. Chimutengwende-Gordon, C. Pendegrass, G. Blunn, Enhancing the soft tissue seal around intraosseous transcutaneous amputation prostheses using silanized fibronectin titanium alloy, Biomed. Mater. 6 (2011) 025008.

[2] C.J. Pendegrass, A.E. Goodship, G.W. Blunn, Development of a soft tissue seal around bone-anchored transcutaneous amputation prostheses, Biomaterials 27 (2006) 4183–4191.

[3] M. Yamada, E. Kato, A. Yamamoto, K. Sakurai, A titanium surface with nano-ordered spikes and pores enhances human dermal fibroblastic extracellular matrix production and integration of collagen fibers, Biomed. Mater. 11 (2016) 015010.

[4] M.G. Yang, P.P. Jiang, Y. Ge, F. Lan, X.D. Zhou, J. He, Y. Wu, Dopamine self-polymerized along with hydroxyapatite onto the preactivated titanium percutaneous implants surface to promote human gingival fibroblast behavior and antimicrobial activity for biological sealing, J. Biomater. Appl. 32 (2018) 1071–1082.

[5] K. Affeld, J. Grosshauser, L. Goubergrits, U. Kertzscher, Percutaneous devices: a review of applications, problems and possible solutions, Expert Rev. Med. Devices 9 (2012) 389–399.

[6] G.J. Chen, Z. Wang, H. Bai, J.M. Li, H. Cai, A preliminary study on investigating the attachment of soft tissue onto micro-arc oxidized titanium alloy implants, Biomed. Mater. 4 (2009) 015017.

[7] K. Li, S.Y. Liu, Y. Xue, L. Zhang, Y. Han, A superparamagnetic Fe₃O₄-TiO₂ composite coating on titanium by micro-arc oxidation for percutaneous implants, J. Mater. Chem. B 7 (2019) 5265–5276.

[8] S. MacNeil, Progress and opportunities for tissue-engineered skin, Nature 445 (2007) 874–880.

[9] M.C.Y. Heng, Wound healing in adult skin: aiming for perfect regeneration, Int. J. Dermatol. 50 (2011) 1058–1066.

[10] P. Martin, Wound healing - aiming for perfect skin regeneration, Science 276 (1997) 75–81.

[11] S.S. Hao, Y. Zhang, J. Meng, J. Liu, T. Wen, N. Gu, H.Y. Xu, Integration of a superparamagnetic scaffold and magnetic field to enhance the wound-healing phenotype of fibroblasts, ACS Appl. Mater. Inter. 10 (2018) 22913–22923.

[12] W.M. Reichert, Indwelling Neural Implants: Strategies for Contending with the in Vivo Environment, CRC Press, Boca Raton, 2008.

[13] S. Sonnylal, S.W. Xu, P. Leoni, K. Naff, C.S. Van Pelt, H. Nakamura, A. Leask, D. Abraham, G. Bou-Gharios, B. de Crombrugghe, Selective expression of connective tissue growth factor in fibroblasts in vivo promotes systemic tissue fibrosis, Arthritis Rheum. 62 (2010) 1523–1532.

[14] J.J. Tomasek, G. Gabbiani, B. Hinz, C. Chaponnier, R.A. Brown, Myofibroblasts and mechano-regulation of connective tissue remodelling, Nat. Rev. Mol. Cell Biol. 3 (2002) 349–363.

[15] K. Li, F. Dai, T. Yan, Y. Xue, L. Zhang, Y. Han, Magnetic silicium hydroxyapatite nanorods for enhancing osteoblast response in vitro and biointegration in vivo, ACS Biomater. Sci. Eng. 5 (2019) 2208–2221.

[16] J.T.B. Ratnayake, M. Mucalo, G.J. Dias, Substituted hydroxyapatites for bone regeneration: a review of current trends, J. Biomed. Mater. Res. B 105 (2017) 1285–1299.

[17] X.L. Fu, M. Xu, J. Liu, Y.M. Qi, S.H. Li, H.J. Wang, Regulation of migratory activity of human keratinocytes by topography of multiscale collagen-containing nanofibrous matrices, Biomaterials 35 (2014) 1496–1506.

[18] J.W. Xie, M.R. MacEwan, W.Z. Ray, W.Y. Liu, D.Y. Siewe, Y.N. Xia, Radially aligned, electrospun nanofibers as dural substitutes for wound closure and tissue regeneration applications, ACS Nano 4 (2010) 5027–5036.

[19] M.A. Surmeneva, T.M. Mukhametkaliyev, A.I. Tyurin, A.D. Teresov, N.N. Koval, T.S. Pirozhkova, I.A. Shuvarin, A.V. Shuklinov, A.O. Zhigachev, C. Oehr, R.A. Surrnenev, Effect of silicate doping on the structure and mechanical properties of thin nanostructured RF magnetron sputter-deposited hydroxyapatite films, Surf. Coat. Technol. 275 (2015) 176–184.

[20] Y. Han, J.H. Zhou, S.M. Lu, L. Zhang, Enhanced osteoblast functions of narrow interligand spaced Sr-HA nano-fibers/rods grown on microporous titania coatings, RSC Adv. 3 (2013) 11169–11184.

[21] L. Zhang, Y. Han, G.X. Tan, Hydroxyaptite nanorods patterned ZrO2 bilayer coating on zirconium for the application of percutaneous implants, Colloids Surf., B 127 (2015) 8–14.

[22] J.Y. Gao, M. Wang, C. Shi, L.P. Wang, D.L. Wang, Y.C. Zhu, Synthesis of trace element Si and Sr codoping hydroxyapatite with non-cytotoxicity and enhanced cell proliferation and differentiation, Biol. Trace Elem. Res. 174 (2016) 208–217.

[23] X.P. Wang, A. Ito, Y. Sogo, X. Li, A. Oyane, Silicate-apatite composite layers on external fixation rods and in vitro evaluation using fibroblast and osteoblast, J. Biomed. Mater. Res. A 92A (2010) 1181–1189.

[24] K.A. Hing, P.A. Revell, N. Smith, T. Buckland, Effect of silicon level on rate, quality and progression of bone healing within silicate-substituted porous hydroxyapatite scaffolds, Biomaterials 27 (2006) 5014–5026.

[25] R.A. Surmenev, M.A. Surmeneva, A.A. Ivanova, Significance of calcium phosphate coatings for the enhancement of new bone osteogenesis- A review, Acta Biomater. 2 (2014) 557–579.

[26] M.A. Surmeneva, A. Kovtun, A. Peetsch, S.N. Goroja, A. Sharonova, V.F. Pichugin, I.Y. Grubova, A.A. Ivanova, A.D. Teresov, N.N. Koval, V. Buck, A. Wittmar, M. Ulbricht, O. Prymak, M. Epple, R.A. Surmenev, Preparation of a silicate-containing hydroxyapatite based coating by magnetron sputtering: structure and osteoblast-like MG63 cells in vitro study, RSC Adv. 3 (2013) 11240–11246.

[27] F.J. Xiao, L. Peng, Y. Zhang, L.J. Yun, Silicon-substituted hydroxyapatite composite coating by using vacuum-plasma spraying and its interaction with human serum albumin, J. Mater. Sci. Mater. Med. 20 (2009) 1653–1658.

[28] D.M. Reffitt, N. Ogston, R. Jugdaohsingh, H.F.J. Cheung, B.A.J. Evans, R.P.H. Thompson, G.N. Hampson, Orthosilicic acid stimulates collagen type 1 synthesis and osteoblastic differentiation in human osteoblast-like cells in vitro, Bone 32 (2003) 127–135 https://sciencedirect.xilesou.top/science/article/abs/pii/S875632820200950X.

[29] Q. Yu, Y. Han, X. Wang, C. Qin, D. Zhai, Z. Yi, J. Chang, Y. Xiao, Chengtie Wu, Copper silicate hollow microspheres-incorporated scaffolds for chemo- photothermal therapy of melanoma and tissue healing, ACS Nano 12 (2018) 2695–2707.

[30] K. Kawai, B.J. Larson, H. Ishise, A.L. Carre, S. Nishimoto, M. Longaker, H.P. Lorenz, Calcium-based nanoparticles accelerate skin wound healing, PLoS One 6 (2011) 27106.

[31] H. Xu, F. Lv, Y. Zhang, Z. Yi, Q. Ke, C. Wu, M. Liu, J. Chang, Hierarchically micropatterned nanofibrous scaffolds with a nanosized bio-glass surface for accelerating wound healing, Nanoscale 7 (2015) 18446–18452.

[32] J.N. Lv, H.W. Li, Y. Mu, S.M. Wang, J. Sun, J. Jiang, P. Ding, B.L. Liu, The adhesion and growth of both the human primary gingival epithelial cells and Streptococcus mutans on micro-arc oxidized titanium, Cell Biochem. Biophys. 70 (2014) 1083–1090.

[33] S.N. Isenhath, Y. Fukano, M.L. Usui, R.A. Underwood, C.A. Irvin, A.J. Marshall, K.D. Hauch, B.D. Ratner, P. Fleckman, J.E. Olerud, A mouse model to evaluate the interface between skin and a percutaneous device, J. Biomed. Mater. Res. A 83A (2007) 915–922.

[34] E.L. Solla, J.P. Borrajo, P. Gonzalez, J. Serra, S. Chiussi, C. Serra, B. Leon, M. Perez-Amor, Pulsed laser deposition of silicon-substituted hydroxyapatite coatings, Vacuum 82 (2008) 1383–1385.

[35] D.K. Pattanayak, T. Kawai, T. Matsushita, H. Takadama, T. Nakamura, T. Kokubo, Effect of HCl concentrations on apatite-forming ability of NaOH-HCl- and heat-treated titanium metal, J. Mater. Sci. Mater. Med. 20 (2009) 2401–2411.

[36] Y. Han, J.H. Zhou, L. Zhang, K.W. Xu, A multi-scaled hybrid orthopedic implant: bone ECM-shaped Sr-HA nanofibers on the microporous walls of a macroporous titanium scaffold, Nanotechnology 22 (2011) 275603.

[37] J.D. Chen, Y.J. Wang, K. Wei, S.H. Zhang, X.T. Shi, Self-organization of hydroxyapatite nanorods through oriented attachment, Biomaterials 28 (2007) 2275–2280.

[38] A. Hasan, V. Saxena, L.M. Pandey, Surface functionalization of Ti6Al4V via self-assembled monolayers for improved protein adsorption and fibroblast adhesion, Langmuir 34 (2018) 3494–3506.

[39] B.G. Keselowsky, D.M. Collard, A.J. Garcia, Surface chemistry modulates fibronectin conformation and directs integrin binding and specificity to control cell adhesion, J. Biomed. Mater. Res. A 66A (2003) 247–259.

[40] J. Zhou, B. Li, S. Lu, L. Zhang, Y. Han, Regulation of osteoblast proliferation and differentiation by interrod spacing of Sr-HA nanorods on microporous titania coatings, ACS Appl. Mater. Interfaces 5 (2013) 5358–5365.

[41] A.B. Nafiu, M.T. Rahman, Selenium added unripe carica papaya pulp extracts enhance wound repair through TGF-beta 1 and VEGF-a signalling pathway, BMC Complement Altern. Med. 15 (2015) 369.

[42] Z.N. Huang, E.R. Nelson, R.L. Smith, S.B. Goodman, The sequential expression profiles of growth factors from osteroprogenitors to osteoblasts *In vitro*, Tissue Eng. 13 (2007) 2311–2320.

[43] R. Narayanan, T.Y. Kwon, K.H. Kim, TiO2 nanotubes from stirred glycerol/NH4F electrolyte: roughness, wetting behavior and adhesion for implant applications, Mater. Chem. Phys. 117 (2009) 460–464.